

77-694

Numerical Solution of Supersonic Laminar Flow Over a Three-Dimensional Compression Corner

C.M. Hung and R.W. MacCormack, *NASA
Ames Research Center, Moffett Field, Ca.*

AIAA 10th FLUID & PLASMADYNAMICS CONFERENCE

Albuquerque, N. Mex./June 27-29, 1977

For permission to copy or republish, contact the American Institute of Aeronautics and Astronautics,
1290 Avenue of the Americas, New York, N.Y. 10019.

M77-15091

AIAA-P-77-694

NUMERICAL SOLUTION OF SUPERSONIC LAMINAR FLOW OVER A THREE-DIMENSIONAL COMPRESSION CORNER

C. M. Hung* and R. W. MacCormack**
Ames Research Center, NASA, Moffett Field, Calif. 94035

Abstract

A newly developed, rapid numerical scheme is extended to three dimensions to solve the complete Navier-Stokes equations for a supersonic, laminar flow over a compression corner with sidewall effects. The program is coded so that it can solve for a general curved ramp surface geometry such as found in inlets and fuselage-wing-flap junctions. A test case of Mach 3.0 flow is calculated. In regions where three-dimensional effects are small, good agreement is obtained between the present calculation and previous two-dimensional solutions. In other regions, the results show complex three-dimensional flow-field interactions including shock-shock and shock/boundary-layer interactions.

Introduction

In the design of an aerodynamic body for supersonic or hypersonic flow, it is important to understand the nature of the flow field developed around the body. One of the most important aspects of the flow is the high heating potential which exists not only in the stagnation regions, but near flow interaction regions as well. Theoretical investigations have some success in predicting the general behavior of such interactions for two-dimensional planar and axisymmetric flows. In the actual design of high-speed vehicles, however, most of the interactions have some degree of three-dimensionality, and a significant number of the interactions cannot be considered two-dimensional even as a first-order approximation.

With recent advances in both computer technology and computational fluid dynamics, routine computations of two-dimensional shock-wave and boundary-layer interactions are now possible. Examples of these computations are included in Refs. 1-5. These studies used MacCormack's⁶ two-step, time-split, explicit, finite-difference scheme to solve the two-dimensional, time-dependent Navier-Stokes equations with various proposed turbulence models. The maximum time step for the explicit scheme was subject to the Courant-Friedrichs-Lewy stability condition. In general, the calculations required large amounts of computer time - 20 min to 3 hr on a CDC 7600, depending upon geometry, Reynolds number, and mesh resolution. However, with the new algorithm developed by MacCormack,^{7,8} the efficiency has been dramatically improved so that the required computer time has been decreased by an order of magnitude, and parametric studies become feasible.⁹

In the present study, the new efficient numerical scheme is extended to three-dimensions to solve the complete Navier-Stokes equations for a supersonic laminar flow over a compression corner with a sidewall (Fig. 1). This configuration is common in many engineering problems, such as inlets,

fuselage-wing-flap junctions, and the intersection of several control surfaces. Inviscid calculations for such geometries have been obtained by Shankar, Anderson, and Kutler.¹⁰ A similar geometry, without the flat plate, was first solved for viscous flow by Shang and Hankey.¹¹ They used the former explicit finite-difference scheme⁶ to solve the problem in a similarity coordinate. Adding the flat plate in front of the wedge complicates the interaction flow field substantially. The wedge shock interacts with boundary layers on both the sidewall and bottom wall, and the flow field near the sidewall-wedge intersection is strongly dominated by the inviscid-viscous interaction. The objectives of the present investigation are: (a) determine the efficiency of the new numerical scheme for solving a three-dimensional problem, and (b) study three-dimensional inviscid-viscous interactions.

Analysis

Numerical Method

Figure 2 shows cross-sections of the computational domain in the (x-y) and (y-z) planes. The mesh is equally spaced in the x-direction, but, in both y- and z-directions, a fine mesh spacing is used in the regions near the wall, $0 < y \leq y_f$ and $0 \leq z \leq z_f$, to resolve the viscous regions, and a coarse mesh spacing is used in the outer regions $y_f \leq y \leq y_h$ and $z_f \leq z \leq z_h$, where viscous effects are negligible. Both the fine and coarse meshes are geometrically stretched with different stretching constants. The minimum mesh spacings for the inner regions, $(\Delta y_i)_{\min}$ and $(\Delta z_i)_{\min}$, are approximately proportional to $L/\sqrt{Re_L}$, depending upon the resolution required, and in the outer regions, the minimum spacings are, for the y-direction,

$$(\Delta y_o)_{\min} = \text{constant} \cdot (y_h - y_f) / (JL - JL_{FM})$$

and, for the z-direction,

$$(\Delta z_o)_{\min} = \text{constant} \cdot (z_h - z_f) / (KL - KL_{FM})$$

Here Re_L is the Reynolds number based on the length, L , from leading edge to corner, and JL_{FM} , KL_{FM} and JL , KL are the number of fine meshes and the total number of mesh points in the y- and z-directions, respectively. The constant is in general positive and less than one. If the constant equals unity, then the outer coarse mesh is equally spaced.

The governing equations of the present analysis are the time-dependent three-dimensional Navier-Stokes equations. The equations are split into three groups corresponding to the coordinate directions, for treatment by three operators: L_x , L_y , and L_z . The conventional explicit two-step numerical scheme⁶ is used in the L_x -operator and in the L_y - and L_z -operators for the outer coarse mesh regions.

*Consultant, DCW Industries. Member AIAA.

**Assistant Chief, Computational Fluid Dynamics Branch. Member AIAA.

$$\begin{aligned} &Lx(0 - y_h, 0 - z_h) \\ &Ly(y_f - y_h, 0 - z_h) \\ &Lz(0 - y_h, z_f - z_h) \end{aligned}$$

where arguments inside the parentheses indicate the regions in which the operators are applied. In the inner regions, the Ly- and Lz-operators are split further into hyperbolic and parabolic operators for the inviscid (Lyh and Lzh) and viscous (Lyp and Lzp) terms

$$\begin{aligned} \text{hyperbolic operator: } &Lyh(0 - y_f, 0 - z_h), \\ &Lzh(0 - y_h, 0 - z_f) \\ \text{parabolic operator: } &Lyp(0 - y_f, 0 - z_h), \\ &Lzp(0 - y_h, 0 - z_f) \end{aligned}$$

With this further splitting, the stable time steps for the inner and outer meshes are about the same, and the complete numerical procedure is now expressed as

$$U^{t+2\Delta t} = (LyLyhLyp) \cdot (LzLzhLzp) \cdot (Lx \cdot Lx) \cdot (LzLzpLzh) \cdot (LyLypLyh)U^t$$

by which the solution is advanced two time steps from t to $t + 2\Delta t$. In the present study, the system of equations is solved in the orthogonal (x, y, z) coordinate system for a general oblique rectangular prism, as shown in Fig. 3. θ is the inclination of the prism and the node point (i, j, k) is located at the centroid of the mesh cell. Based upon the concept of splitting,¹² the extension of the numerical scheme to multidimensions is very straightforward; the Lzh- and Lzp-operators are essentially the logical extension to three-dimensional flow of those discussed in Refs. 7 and 8. Here, we briefly describe the extension of Lyh- and Lyp-operators to a general oblique prism in three dimensions.

Lyh Operator

To account for the inviscid terms in the y -direction, the Lyh-operator solves the split conservation law "equations"

$$\frac{\partial U}{\partial t} + \frac{\partial G_H}{\partial y} = 0 \quad (1)$$

where

$$U = \begin{bmatrix} \rho \\ \rho u \\ \rho v \\ \rho w \\ E \end{bmatrix} \quad G_H = \begin{bmatrix} \rho(v - u \tan \theta) \\ \rho u(v - u \tan \theta) - p \tan \theta \\ \rho v(v - u \tan \theta) + p \\ \rho w(v - u \tan \theta) \\ (E + p) \cdot (v - u \tan \theta) \end{bmatrix}$$

Here p, ρ, E are the fluid properties (pressure, density, and total energy), with $E = \rho[e_1 + 1/2(u^2 + v^2 + w^2)]$, where e_1 is the specific internal energy, and (u, v, w) are the velocity components in the (x, y, z) directions. Conventional explicit-difference schemes for solving these equations are limited by the CFL condition

$$\Delta t \leq \frac{\Delta y}{|v - u \tan \theta| + c \sec \theta}$$

where c is sound speed. In the Lyh-operator, the convection velocity, $v - u \tan \theta$, and pressure, p , are first predicted at time $t + \Delta t$ by the method of characteristics. Equation (1) is then solved by the two-step predictor-corrector scheme with the stability time-step restriction

$$\Delta t \leq \frac{\Delta y}{|v - u \tan \theta|}$$

which is substantially larger than that allowed by the usual CFL stability condition in a thin, fine-mesh shear layer near the wall.

To derive the characteristic relations, we first write Eq. (1) in nonconservative form

$$\frac{\partial}{\partial t} \begin{bmatrix} \rho \\ v' \\ w \\ p \end{bmatrix} + \begin{bmatrix} v' & \rho & 0 & 0 \\ 0 & v' & 0 & \frac{1 + \tan \theta}{\rho} \\ 0 & 0 & v' & 0 \\ 0 & p & 0 & v' \end{bmatrix} \frac{\partial}{\partial y} \begin{bmatrix} \rho \\ v' \\ w \\ p \end{bmatrix} = 0 \quad (2)$$

where $v' = v - u \tan \theta$, $p = (\gamma - 1)\rho e_1$, and γ is the ratio of specific heat. Then, along the characteristics

$$\xi_{\pm} = y - (v' \pm c \sec \theta)t = \text{constant}$$

the compatibility relations are

$$dp \pm \rho c \cos \theta dv' = 0$$

Shown in Fig. 4 is a sketch of the characteristics. The index j refers to the point (i, j, k) in three-dimensions. This convention is used throughout the present discussion. Through the point $(j, t + \Delta t)$, there are two characteristics, one of ξ_+ -type and one of ξ_- -type, which intersect the known data line at A and B. The values of v_j^* and p_j^* at $t + \Delta t$ can then be calculated from the compatibility relations along the characteristics. In the present study, the values of v_j^* and p_j^* are calculated by space-averaging over the time from t to $t + 2\Delta t$. Thus,

$$\begin{aligned} p_j^* &= \frac{p_j^+ + p_j^-}{2} + \rho_j c_j \cos \theta \frac{v_j^+ - v_j^-}{2} \\ v_j^{*,*} &= \frac{v_j^+ + v_j^-}{2} + \frac{1}{\rho_j c_j \cos \theta} \frac{p_j^+ - p_j^-}{2} \end{aligned}$$

where

$$\begin{aligned} p_j^+ &= \frac{1}{L^+} \sum_k p_{j-k} \Delta y_k, & v_j^+ &= \frac{1}{L^+} \sum_k v_{j-k} \Delta y_k \\ p_j^- &= \frac{1}{L^-} \sum_m p_{j+m} \Delta y_m, & v_j^- &= \frac{1}{L^-} \sum_m v_{j+m} \Delta y_m \\ L^+ &= \sum_k \Delta y_k, & L^- &= \sum_m \Delta y_m \end{aligned}$$

and, Δy_k and Δy_m are the averaging weight factors which, except at the end points as shown in Fig. 4,

are mesh cell widths. The time-averages of gradients of v'_j and p_j are evaluated, from Eq. (2),

$$\left. \begin{aligned} (1 + \tan^2 \theta) \left(\frac{\partial \bar{p}}{\partial y} \right)_j &= - \frac{1}{\Delta t \rho} \int_t^{t+\Delta t} \left(\frac{\partial}{\partial t} + v' \frac{\partial}{\partial y} \right) v' dt \\ &= - \frac{1}{\Delta t \rho_j} \left[(v_j^{*+} - v_j^{*-}) \right. \\ &\quad \left. + \frac{v_j^{*+} + v_j^{*-}}{2} \frac{v_j^{*-} - v_j^{*+}}{2c_j \sec \theta} \right] \\ \left(\frac{\partial \bar{v}'}{\partial y} \right)_j &= - \frac{1}{\gamma p \Delta t} \int_t^{t+\Delta t} \left(\frac{\partial}{\partial t} + v' \frac{\partial}{\partial y} \right) p dt \\ &= - \frac{1}{\gamma p_j \Delta t} \left[(p_j^{*+} - p_j^{*-}) \right. \\ &\quad \left. + \frac{v_j^{*+} + v_j^{*-}}{2} \frac{p_j^{*-} - p_j^{*+}}{2c_j \sec \theta} \right] \end{aligned} \right\} (3)$$

Integrating the time-averaged gradients, Eq. (3), in y , we have time-averaged values of \bar{v}' and \bar{p} at $t + (1/2)\Delta t$,

$$\bar{v}' = \int_0^y \left(\frac{\partial \bar{v}'}{\partial y} \right) dy$$

$$\bar{p} = p_{\text{wall}} + \int_0^y \left(\frac{\partial \bar{p}}{\partial y} \right) dy$$

Now Eq. (1) can be integrated in time from t to $t + \Delta t$ by the conventional predictor-corrector scheme, except that $v' = v - u \tan \theta$ and p are replaced by their time-averaged values \bar{v}' and \bar{p} .

Lyp Operator

To solve the viscous terms in the inner regions the Lyp-operator solves the following "equations"

$$\left. \begin{aligned} \frac{\partial \rho}{\partial t} &= 0 \\ \frac{\partial u}{\partial t} &= \frac{1}{\rho} \frac{\partial}{\partial y} [\tau_{xy} - \tan \theta \sigma_x] \\ \frac{\partial v}{\partial t} &= \frac{1}{\rho} \frac{\partial}{\partial y} [\sigma_y - \tan \theta \tau_{xy}] \\ \frac{\partial w}{\partial t} &= \frac{1}{\rho} \frac{\partial}{\partial y} [\tau_{yz} - \tan \theta \tau_{xz}] \\ \frac{\partial}{\partial t} \left[e_1 + \frac{1}{2} (u^2 + v^2 + w^2) \right] \\ &= \frac{1}{\rho} \frac{\partial}{\partial y} \left[u \tau_{xy} + w \tau_{yz} + v \sigma_y + \frac{\gamma \mu}{Pr} \frac{\partial e_1}{\partial y} \right. \\ &\quad \left. - \tan \theta \left(u \sigma_x + v \tau_{xy} + w \tau_{xz} + \frac{\gamma \mu}{Pr} \frac{\partial e_1}{\partial x} \right) \right] \end{aligned} \right\} (4)$$

where

$$\sigma_x = \lambda \left(\frac{\partial u}{\partial x} + \frac{\partial v}{\partial y} + \frac{\partial w}{\partial z} \right) + 2\mu \frac{\partial u}{\partial x}$$

$$\sigma_y = \lambda \left(\frac{\partial u}{\partial x} + \frac{\partial v}{\partial y} + \frac{\partial w}{\partial z} \right) + 2\mu \frac{\partial v}{\partial y}$$

$$\tau_{xy} = \mu \left(\frac{\partial u}{\partial y} + \frac{\partial v}{\partial x} \right)$$

$$\tau_{xz} = \mu \left(\frac{\partial u}{\partial z} + \frac{\partial w}{\partial x} \right)$$

$$\tau_{yz} = \mu \left(\frac{\partial v}{\partial y} + \frac{\partial w}{\partial z} \right)$$

Note that σ_x and σ_y are normal stresses in the x - and y -directions, respectively, without the pressure term. In the present investigation the viscosity coefficient, μ , is assumed to be a function of temperature only, and is evaluated by Sutherland's empirical formula. The second viscosity coefficient $\lambda = -(2/3)\mu$, and the Prandtl number, Pr , is a constant equal to 0.72.

Variable and coordinate transformations are introduced

$$\begin{aligned} u' &= u + v \tan \theta & \xi &= x \\ v' &= v - u \tan \theta & \eta &= y - b(x), \quad b'(x) = \tan \theta \\ w' &= w & \zeta &= z \end{aligned}$$

and Eq. (4) can be rewritten as

$$\frac{\partial \rho}{\partial t} = 0$$

$$\frac{\partial u'}{\partial t} - \frac{1}{\rho} \frac{\partial}{\partial \eta} \left[\mu \sec^2 \theta \frac{\partial u'}{\partial \eta} \right] = \frac{1}{\rho} \frac{\partial}{\partial \eta} G_1$$

$$\frac{\partial v'}{\partial t} - \frac{1}{\rho} \frac{\partial}{\partial \eta} \left[(\lambda + 2\mu) \sec^2 \theta \frac{\partial v'}{\partial \eta} \right] = \frac{1}{\rho} \frac{\partial}{\partial \eta} G_2$$

$$\frac{\partial w'}{\partial t} - \frac{1}{\rho} \frac{\partial}{\partial \eta} \left[\mu \sec^2 \theta \frac{\partial w'}{\partial \eta} \right] = \frac{1}{\rho} \frac{\partial}{\partial \eta} G_3$$

$$\frac{\partial u'^2}{\partial t} - \frac{1}{\rho} \frac{\partial}{\partial \eta} \left[\mu \sec^2 \theta \frac{\partial u'^2}{\partial \eta} \right] = \frac{2}{\rho} \frac{\partial}{\partial \eta} u' G_1 - 2\phi_\xi$$

$$\frac{\partial v'^2}{\partial t} - \frac{1}{\rho} \frac{\partial}{\partial \eta} \left[(\lambda + 2\mu) \sec^2 \theta \frac{\partial v'^2}{\partial \eta} \right] = \frac{2}{\rho} \frac{\partial}{\partial \eta} v' G_2 - 2\phi_\eta$$

$$(4) \quad \frac{\partial w'^2}{\partial t} - \frac{1}{\rho} \frac{\partial}{\partial \eta} \left[\mu \sec^2 \theta \frac{\partial w'^2}{\partial \eta} \right] = \frac{2}{\rho} \frac{\partial}{\partial \eta} w' G_3 - 2\phi_\zeta$$

$$\frac{\partial e_1}{\partial t} - \frac{1}{\rho} \frac{\partial}{\partial \eta} \left[\frac{\gamma \mu}{Pr} \sec^2 \theta \frac{\partial e_1}{\partial \eta} \right] = \frac{1}{\rho} \frac{\partial}{\partial \eta} G_4$$

$$+ \cos^2 \theta (\phi_\xi + \phi_\eta) + \phi_\zeta$$

where

$$G_1 = \mu \frac{\partial}{\partial \xi} (v' - u' \tan \theta)$$

$$G_2 = \lambda \left[\frac{\partial}{\partial \xi} (u' - v' \tan \theta) + \cos^2 \theta \frac{\partial w'}{\partial \xi} \right] \sec^2 \theta - 2 \tan \theta \mu \frac{\partial v'}{\partial \xi}$$

$$G_3 = \mu \left(\frac{\partial v'}{\partial \xi} - \frac{\partial w'}{\partial \xi} \tan \theta \right)$$

$$G_4 = -\frac{\gamma \mu}{Pr} \tan \theta \frac{\partial e_1}{\partial \xi}$$

$$\phi_\xi = \left[\mu \sec^2 \theta \frac{\partial u'}{\partial \eta} + G_1 \right] \frac{1}{\rho} \frac{\partial u'}{\partial \eta}$$

$$\phi_\eta = \left[(\lambda + 2\mu) \sec^2 \theta \frac{\partial v'}{\partial \eta} + G_2 \right] \frac{1}{\rho} \frac{\partial v'}{\partial \eta}$$

$$\phi_\zeta = \left[\mu \sec^2 \theta \frac{\partial w'}{\partial \eta} + G_3 \right] \frac{1}{\rho} \frac{\partial w'}{\partial \eta}$$

The continuity equation has no viscous term, and, hence, is trivial to solve. It implies that density is constant in time in the parabolic operator. In the transformed variable, v' is the velocity component normal to the plane $\eta = \text{constant}$, and, in general, is small compared to u' . The G_1 , G_2 , G_3 , G_4 terms are cross derivatives and ϕ_ξ , ϕ_η , ϕ_ζ are the dissipation terms of (u'^2, v'^2, w'^2) kinetic energy equations. The internal energy equation is obtained by subtracting the three kinetic energy equations from the total energy equation. Treating the right-hand side explicitly, each equation of the system is a typical uncoupled "heat transfer" model parabolic equation, and can be efficiently solved by either Crank-Nicholson or Laasonen implicit difference scheme, using a simple tridiagonal inversion. The present method first solves the three momentum equations, and uses the calculated u' , v' , w' values to evaluate the dissipation terms ϕ_ξ , ϕ_η , and ϕ_ζ . Details of the numerical procedure are discussed in Refs. 7 and 8.

Boundary Conditions and Special Considerations

The upstream boundary is located either a few points ahead of the leading edge with uniform supersonic free-stream conditions (M_∞ , u_∞ , p_∞ , ρ_∞) or ahead of the wedge shock with the flow conditions generated from the present program by solving the Navier-Stokes equations over an axial corner.

The downstream and far-field boundaries are positioned far enough from the three-dimensional interaction region so that zero-flow-gradient boundary conditions may be used in each coordinate direction. At $z = z_h$, we may also apply the symmetric conditions which are equivalent to flow in a channel. (Effects of these zero-gradient boundary conditions at the far field will be examined later in the Discussion Section.) Both the sidewall and bottom wall are assumed impermeable, and no-slip boundary conditions are applied. The wall is taken to be either isothermal or adiabatic, and the wall pressure is treated simply as

$$\frac{\partial p}{\partial y} = 0 \quad \text{at } y = 0$$

$$\frac{\partial p}{\partial z} = 0 \quad \text{at } z = 0$$

For our present case, the wedge angle is small, the walls are flat, and the first mesh point is close to the wall so that these pressure conditions are appropriate. During the calculations within the inner mesh, the flux and stress terms at the internal boundaries ($y = y_f$ and $z = z_f$) are saved, and their net quantities are then used as boundary conditions for the outer mesh flow calculations.

One of the major difficulties of three-dimensional calculations is the computer-storage requirement. Extension from a two-dimensional set of $(n \times n)$ mesh points to a three-dimensional set of $(n \times n \times n)$ mesh points increases the required data storage by about a factor of 1.2 n . In the present study, the nonconservative variables (u , v , w , e_1) are updated after each column sweep of the split operator. Therefore, the storage required for the conservative variables (ρ , ρu , ρv , ρw , E) is one time level plus one extra column for the predictor and corrector values, instead of two complete time levels of data. The storage requirement is thus reduced by about a factor of 1.5. With this procedure, the updated values are used in the evaluation of the viscous cross-derivative terms.

Results and Discussions

To our knowledge, there is no experimental measurement of supersonic laminar flow for the present geometry. To establish the validity of the numerical code, a test case was calculated. The flow conditions, which corresponded identically to one of the cases studied in Refs. 13 and 14 (with the addition of sidewall), are

$$\begin{aligned} M_\infty &= 3.0 & Re_L &= 1.68 \times 10^4 & \alpha &= 10^\circ \\ T_\infty &= 390^\circ & L &= 0.2 \text{ ft} & & \text{adiabatic walls} \end{aligned}$$

Figure 5 shows a $(y-z)$ cross-section of the mesh. For both the y - and z -directions, a total of 30 mesh points were used, 18 for the fine mesh and 12 for the coarse mesh. For the fine mesh, the stretching constant was calculated such that $\Delta y_1)_{\min} = \Delta z_1)_{\min} = L/(2\sqrt{Re_L})$ and the internal mesh boundaries were placed at $y_f = z_f = 0.017$ ft. The outer coarse mesh was equally spaced with outer boundaries at $y_h = z_h = 0.12$ ft. There were also 30 mesh points in the x -direction. We first calculated the flow from $x/L = -0.061$ to $x/L = 0.646$, and then, using these results for upstream boundary conditions, we calculated the flow from $x/L = 0.525$ to $x/L = 1.628$. The time steps were limited by the CFL condition of the Lx operator and were about $\Delta t_1 = 0.12 \times 10^{-5}$ sec for the first calculation, and $\Delta t_2 = 0.19 \times 10^{-5}$ sec for subsequent calculation. Both regions took about 300 time steps to reach steady-state solutions.

Figure 6 compares previous two-dimensional solutions¹⁴ with present results for u -velocity profiles at two locations where three-dimensional effects are small. The agreement is excellent. Figure 7 shows density contours in an $(x-y)$ plane near the leading edge. Bow shocks from both flat

plates are evident. The intersection of these two bow shocks is also shown in a (y-z) plane, Fig. 8. Upstream of the influence of the wedge, the axial corner-flow solution is symmetric along the 45° plane. The leading-edge shocks are very weak, and we were unable to clearly resolve the detailed structure of their intersection. Figures 9a and 9b show isobars in (x-y) planes at $z = 0$ (sidewall) and $z/z_h = 0.821$ (outer region). The wedge shock is well formed in the outer region, but, on the sidewall, the pressure force diffuses over quite a large region. This diffusion occurs, first of all, because the flow is laminar and the boundary layer is very thick, and, second, because the mechanism to balance the pressure gradient in the y-direction is very weak. (This is discussed later.) The density and pressure contours in a (y-z) plane in the downstream region at $x/L = 1.59$ (Figs. 10a and 10b) demonstrate the interaction of a skewed wedge shock with the sidewall boundary layer. The high pressure in the inner axial region compresses the boundary layer on the sidewall (see Fig. 10a). Also, the flow is forced upward by the diffused pressure gradient on the sidewall; this action thickens the boundary layer away from the axial corner. The diffusion of the wedge shock, as it approaches the sidewall is observed in Fig. 10b. One should note that the isobars near the axial corner are bent downward, similar to those shown in Ref. 15. The bending downward of the locus of the strong pressure gradient is due to the process of expansion (or diffusion) of high pressure under the wedge shock to the outside low-pressure region through the sidewall boundary layer. This is shown in the plot of pressure profile at $z = 0$ in Fig. 10b.

Unlike a pressure force propagating against the stream in the x-direction which retards the flow, the pressure gradient in the y-direction bends the stream in that direction. It takes a long distance before the skin friction and the inertial forces from the surrounding fluid damp out the y-momentum generated by the lateral pressure force. This can be seen in Fig. 11a which shows the u- and v-velocity profiles across the sidewall boundary layer. Even far above the inviscid shock, $y/y_s = 3.0$, the cross-flow v-velocity, at $z/z_h = 0.05$, can be as large as 12.5% of free-stream velocity, and the streamline deflection angle, Fig. 11b, is as large as 56° at $z = 0$. As z increases, the u-momentum increases so that the deflection angle required to balance the pressure force is decreased. This leads to a typical three-dimensional feature of the flow field; the flow direction is skewed across a three-dimensional boundary layer.

We also note, as shown in Figs. 12 and 13, that, while the surface pressures on the flat plate and wedge surface are relatively insensitive to the three-dimensional geometry, the u-velocity separation and reattachment lines on the $y = 0$ surface show strong three-dimensional effects because of the influence of the sidewall. In the downstream region the pressure, Fig. 12, is lower along the axial corner than in the outer region because of the diffusion of the wedge shock discussed earlier. Although the overall static pressure rise is smaller in the axial corner region, the fluid momentum is weaker and, hence, the separation region is larger. However, the sidewall boundary layer and separation results in a fencing effect which forces the flow outward in the z-direction and makes the flow more

difficult to separate in a region near the sidewall. Farther away, the flow approaches a two-dimensional solution. These features are similar to the sketch of a typical oil-film-accumulation line shown in Ref. 16.

To test the effect of the zero-gradient outer boundary conditions at $y = y_h$ and $z = z_h$, the computational domain was extended from $y_h = z_h = 0.12$ ft to $y_h = z_h = 0.19$ ft, about a factor of 2.5 increase in cross-sectional area. A total of (31,31,31) mesh points was used, with the outer mesh stretched geometrically. Figure 14 shows pressure contours for the new results which reproduce all the features in Fig. 10b, and, in addition, a larger area. This confirms the hypothesis that the boundary layers around $y = y_h$ and $z = z_h$ are parabolic, and the assumed zero-gradient boundary conditions do not introduce significant errors in the region of interest. It is interesting to note that the deflection of the pressure and density contours near the outer region $z = z_h$ in Figs. 10a and 10b is physically associated with bow shock from the sidewall leading edge. This also explains the differences in surface pressure and u-velocity separation and reattachment (Figs. 12 and 13) between the outer region three-dimensional solutions and the previous two-dimensional results.¹⁴

The present program is coded so that it can solve a general curved wall in the $y = 0$ plane. Calculations using a $30 \times 30 \times 30$ mesh take about 1.2 hr on a CDC 7600 for 300 time steps. Shang and Hankey,¹¹ while solving a similar geometry without the flat-plate portion, took about 10 hr of CDC 7600 CPU time for a $8 \times 32 \times 36$ mesh and 6000 time steps.

Concluding Remarks

A supersonic laminar flow over a three-dimensional corner has been numerically simulated by solving the complete three-dimensional Navier-Stokes equations with appropriate boundary conditions. The results demonstrate complex three-dimensional flow-field features including shock-shock and shock/boundary-layer interactions. The pressure gradient on the sidewall generated by the skewed wedge shock extends over a large area. The computation time for the present method is nearly independent of Reynolds numbers; hence, it may be extended to turbulent flow calculation without a drastic increase in computation time.

References

- ¹Baldwin, B. S. and MacCormack, R. W., "Interaction of Strong Shock Wave with Turbulent Boundary Layer," AIAA Paper 74-558, Palo Alto, Calif., June 1974.
- ²Shang, J. S. and Hankey, W. L., "Numerical Solution for Supersonic Turbulent Flow over a Compression Ramp," AIAA Journal, Vol. 13, No. 10, Oct. 1975, pp. 1368-1374.
- ³Deiwert, G. S., "Computation of Separated Transonic Turbulent Flows," AIAA Journal, Vol. 14, No. 6, June 1976, pp. 735-741.

⁴Mateer, G. G., Brosh, A., and Viegas, J. R., "A Normal Shock-Wave Turbulent Boundary-Layer Interaction at Transonic Speeds," AIAA Paper 76-161, Washington, D.C., Jan. 1976.

⁵Hung, C. M. and MacCormack, R. W., "Numerical Simulation of Supersonic and Hypersonic Turbulent Compression Corner Flows," AIAA Journal, Vol. 15, No. 3, March 1977, pp. 410-416.

⁶MacCormack, R. W. and Baldwin, B. S., "A Numerical Method for Solving the Navier-Stokes Equations with Application to Shock-Boundary Layer Interactions," AIAA Paper 75-1, Pasadena, Calif., Jan. 1975.

⁷MacCormack, R. W., "An Efficient Numerical Method for Solving the Time-Dependent Compressible Navier-Stokes Equations at High Reynolds Number," NASA TM X-73,129, July 1976.

⁸MacCormack, R. W., "An Efficient Explicit-Implicit Numerical Scheme for Solving the Compressible Navier-Stokes Equations," (to be presented at the 744th Meeting of the American Mathematical Society, New York, N. Y., April 1977).

⁹Horstman, C. C., Settles, G. S., Vas, I. E., Bogdonoff, S. M., and Hung, C. M., "Reynolds Number Effects on Shock-Wave Turbulent Boundary Layer Interactions - A Comparison of Numerical and Experimental Results," AIAA Paper 77-42, Los Angeles, Calif., Jan. 1977.

¹⁰Shankar, V., Anderson, D., and Kutler, P., "Numerical Solutions for Supersonic Corner Flow," Journal of Computational Physics, Vol. 17, No. 2, July 1975, pp. 160-180.

¹¹Shang, J. S. and Hankey, W. L., "Numerical Solution of Compressible Navier-Stokes Equations for a Three-Dimensional Corner," AIAA Paper 77-169, Los Angeles, Calif., Jan. 1977.

¹²Lomax, H., "Recent Progress in Numerical Techniques for Flow Simulation," AIAA Journal, Vol. 14, No. 4, April 1976, pp. 512-518.

¹³Carter, J. E., "Numerical Solutions of the Navier-Stokes Equations for Supersonic Laminar Flow Over a Two-Dimensional Compression Corner," NASA TR R-385, July 1972.

¹⁴Hung, C. M. and MacCormack, R. W., "Numerical Solutions of Supersonic and Hypersonic Laminar Compression Corner Flows," AIAA Journal, Vol. 14, No. 4, April 1976, pp. 475-481.

¹⁵Charwat, A. F. and Redekopp, L. G., "Supersonic Interference Flow Along the Corner of Intersecting Wedge," AIAA Journal, Vol. 5, No. 3, March 1967.

¹⁶Chapman, D. R., Kuehn, D. M., and Larson, H. K., "Investigation of Separated Flows in Supersonic and Subsonic Streams with Emphasis on the Effect of Transition," NACA Report 1356, 1958.

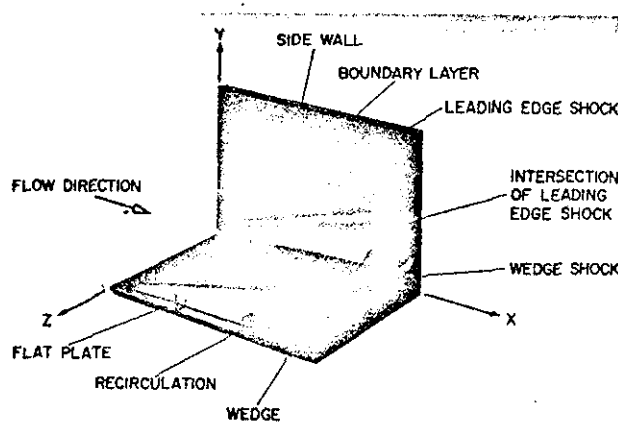


Fig. 1 Three-dimensional compression corner.

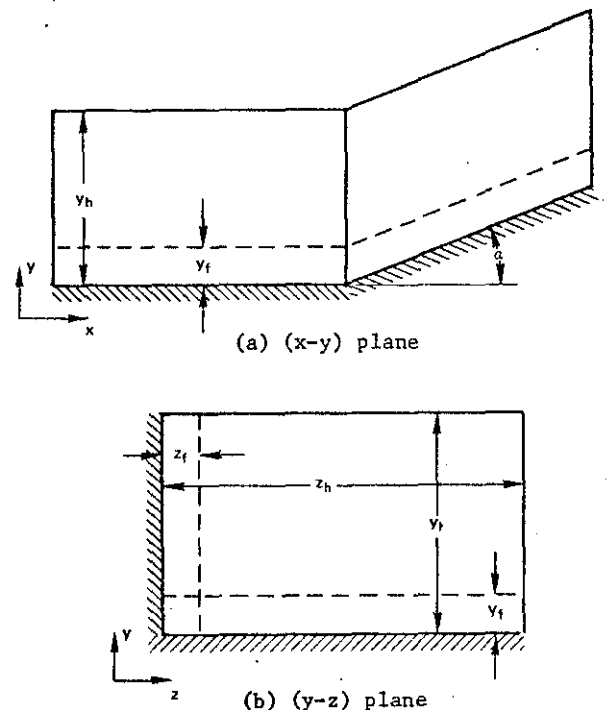


Fig. 2 Cross-sectional views of the computational domain.

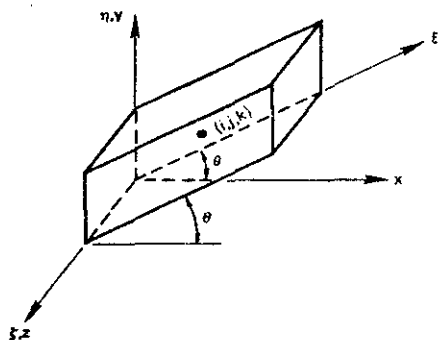


Fig. 3 Oblique rectangular prism element of three-dimensional mesh.

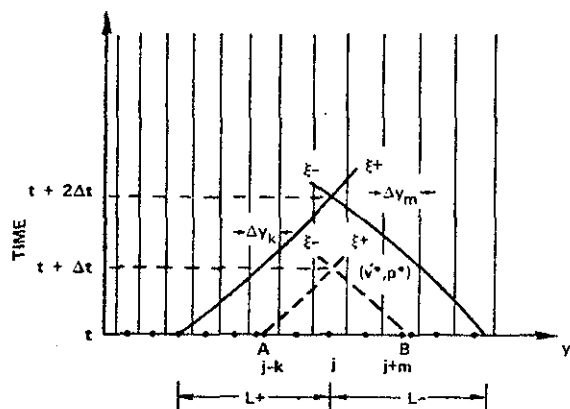


Fig. 4 Sketch of characteristics in $(y-t)$ plane.

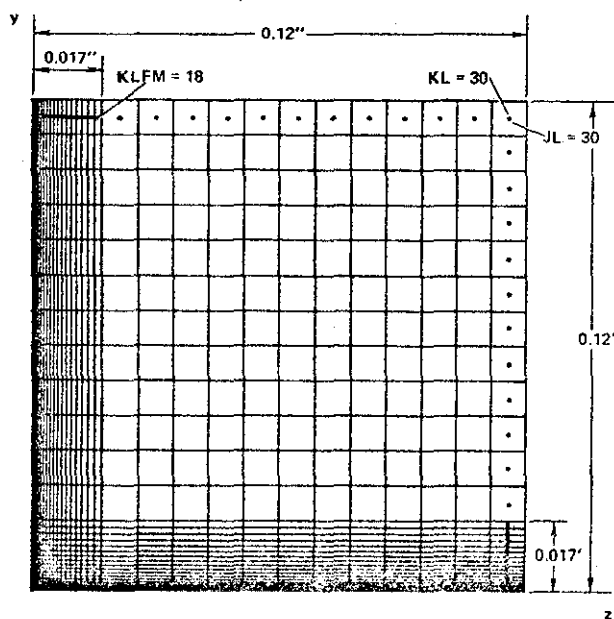


Fig. 5 Details of "mesh" cells in $(y-z)$ plane.

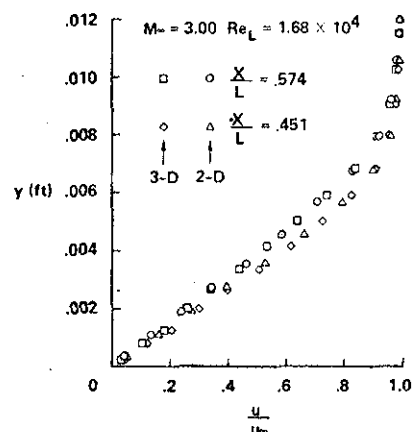


Fig. 6 Flat-plate solutions.

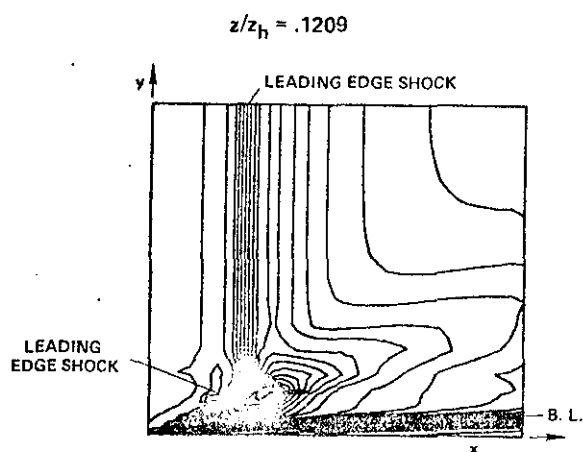


Fig. 7 Density contours in $(x-y)$ plane at $z/z_h = 0.1209$.

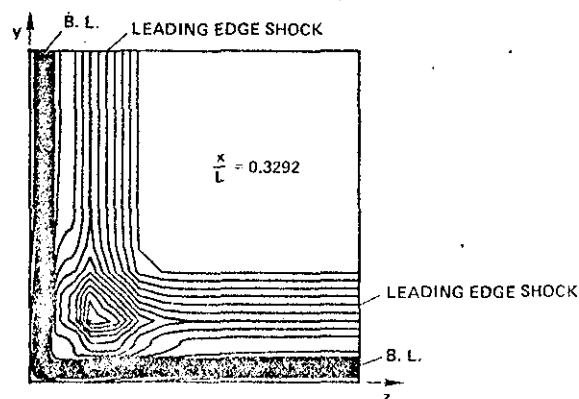


Fig. 8 Density contours in $(y-z)$ plane at $x/L = 0.3292$.

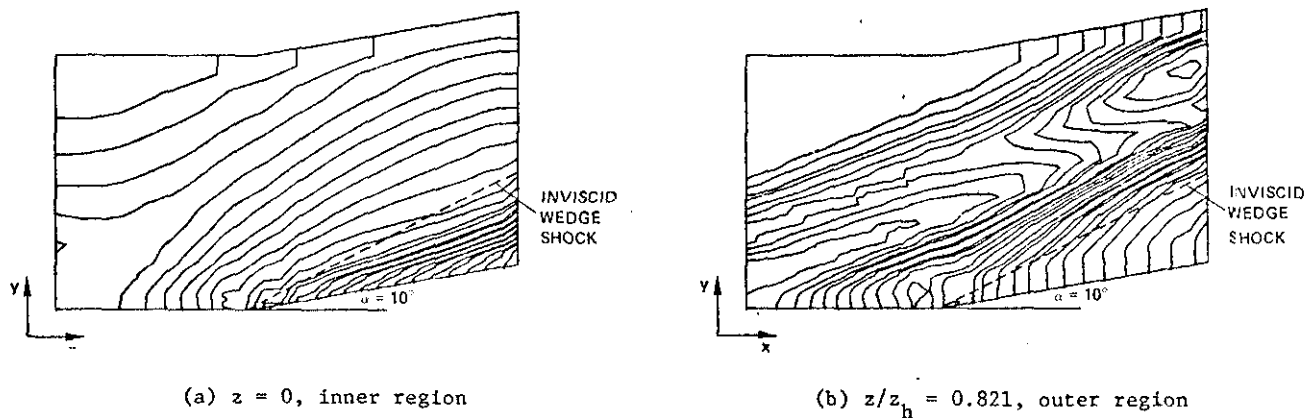


Fig. 9 Isobars on two (x-y) planes.

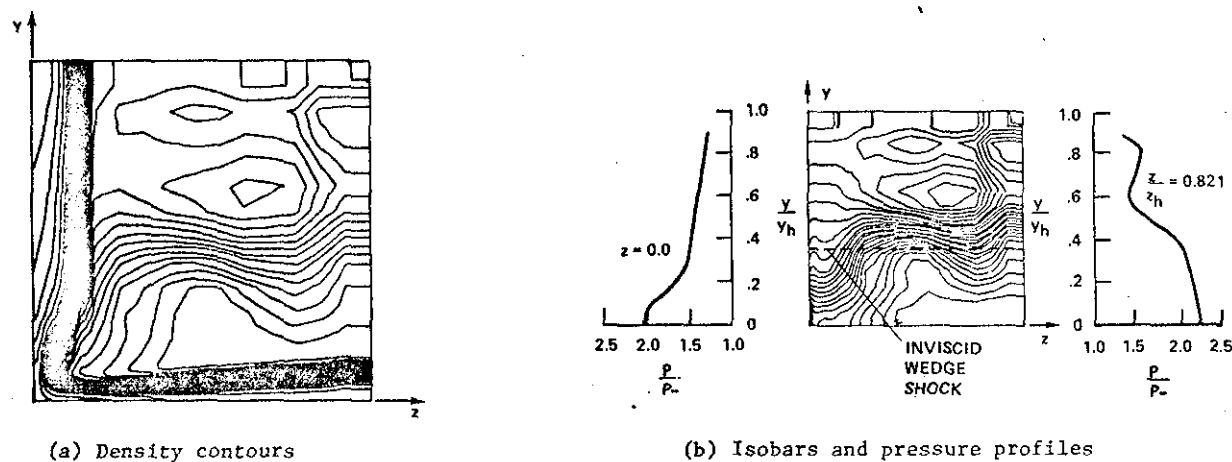


Fig. 10 Density and pressure contours in (y-z) plane at $x/L = 1.590$.

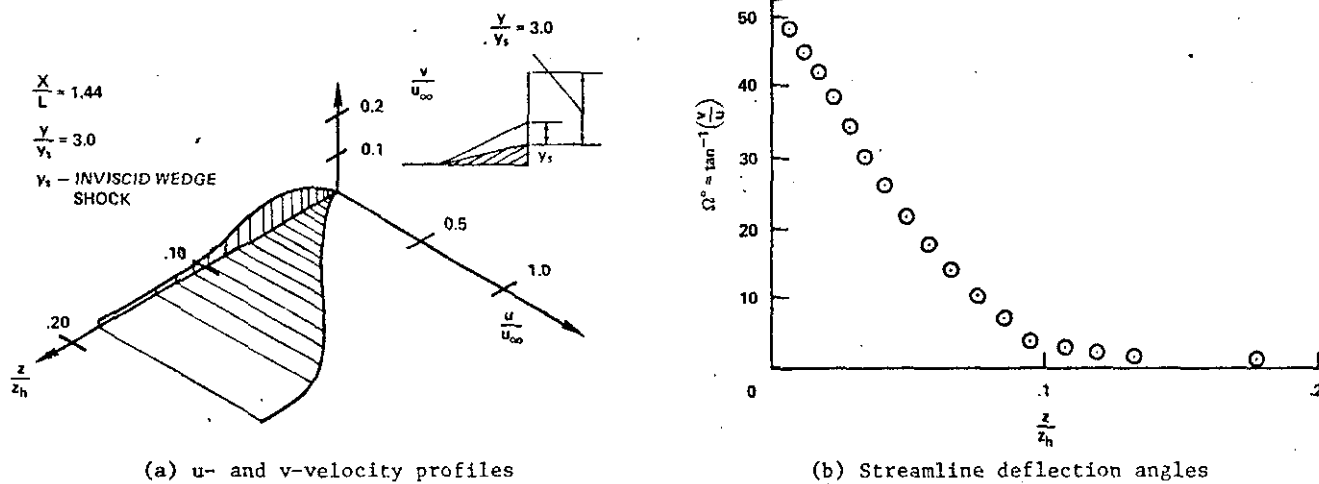


Fig. 11 Velocity profiles and deflection angle across sidewall boundary layer.

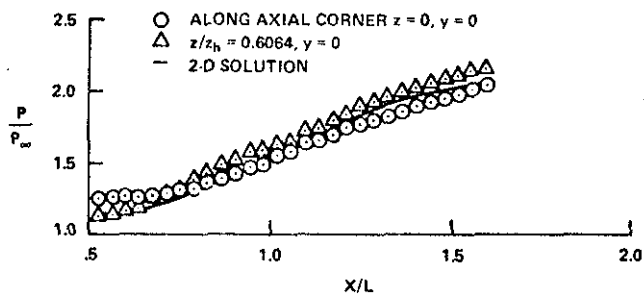


Fig. 12 Comparison of surface pressure on $y = 0$, with two-dimensional result.

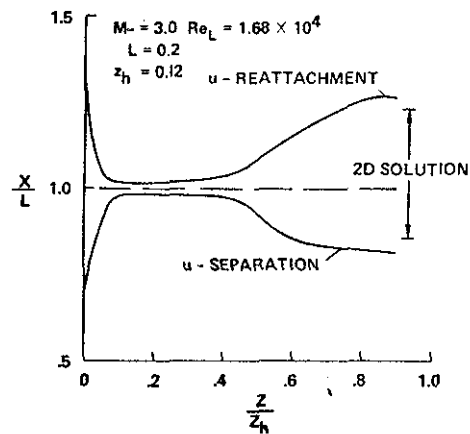


Fig. 13 u -velocity separation and reattachment on $y = 0$ plane.

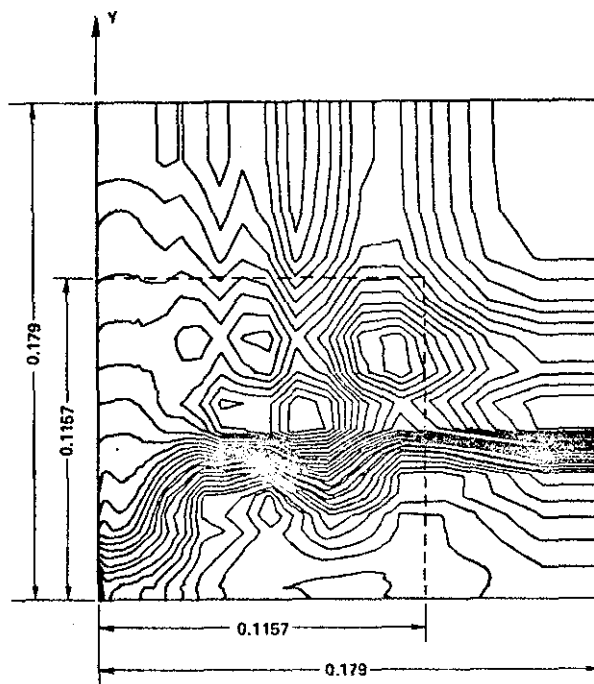


Fig. 14 Isobars of a $(y-z)$ plane at $x/L = 1.59$ with $y_h = z_h = 0.19$ ft.